

NEMS diaphragm sensors integrated with triple-nano-ring resonator

Bo Li, Chengkuo Lee*

Department of Electrical and Computer Engineering, National University of Singapore, 4 Engineering Drive 3, Singapore 117576, Singapore

ARTICLE INFO

Article history:

Available online 25 February 2011

Keywords:

Photonic crystal
Sensors
Ring resonators
Filters

ABSTRACT

Two types of circular diaphragm, made by Si and Si/SiO₂, integrated with hexagonal photonic crystal (PhC) lattice with triple-nano-ring (TNR) resonator created at the centre are proposed as nano-scale force and pressure sensor. The optimized channel drop effect of the TNR resonator brings a strong forward drop resonant peak in both the cases and with Q-factor of 1602 and 1737, respectively. The resonant wavelength peak experience red shifts upon the applied load on the circular diaphragm along the normal direction, in terms of a 2nd-order polynomial relationship. The devices can detect a wide range of applied load. Si diaphragm based micro force sensor gives minimum detectable force of 0.847 μN in the region of applied force from 10 to 20 μN. Si/SiO₂ diaphragm based pressure sensor gives minimum detectable pressure of 4.17 MPa in the region of applied pressure from 20 to 40 MPa. From the derived wavelength shift versus a given centre displacement of the diaphragm, Si diaphragm based sensor shows higher sensitivity than Si/SiO₂ diaphragm sensor.

© 2011 Elsevier B.V. All rights reserved.

1. Introduction

There are many examples of micromachined mechanical sensors in the force sensing and pressure sensing. As one of the first developed MEMS devices, for more than four decades, microelectromechanical systems (MEMS) based pressure sensors have continuously evolved from the original approach using piezoresistive into many other kinds of sensing mechanisms such as, piezoelectric, capacitive, resonant and optical. Most of the well-known transducer configurations for pressure sensing are relying on a free-standing deformable diaphragm [1,2]. Due to the significant technological progress in the micro/nano-fabrication, nanoelectromechanical systems (NEMS) based sensors have attracted major research attention in the past few years. Bio/chemical sensors, e.g. DNA sensing, and nanomechanical sensors, e.g. force and pressure sensing, deploying carbon nanotubes (CNTs) or silicon nanowires have been reported [2–7]. By leveraging the small footprint of NEMS sensors, such solutions show advantages in the implanted biomedical sensing applications, for examples, blood flow measurement, guidewire based pressure sensing, and intraocular pressure sensing, etc. [8–11].

During the last decades, since the pioneering work of photonic band gap (PBG) and PhCs done by the Yablonovitch [12] and John [13], it has received considerable attention for the fundamental physics study as well as various potential applications. The PhCs are engineered nanostructures which are capable of

controlling and manipulating the propagation of electromagnetic waves within a certain frequency range. Various integrated nanophotonics devices have been proposed, such as channel drop filters [14], power splitters [15], directional couplers [16–18] and so on. Micro-ring resonator device is a well-known approach to achieve channel drop filter with high quality [19–22]. The ultimate sizes of such PhC filters are suggested to be less than 1/10,000 of those of conventional optical devices. Hence, PhCs devices can achieve same function with ultra-small size due to their nanometer scale so as to raise channel densities within a small chip of photonic ICs. By leveraging the NEMS technology, the integration of silicon PhCs based nano-cavity resonators and/or nano-ring resonators on silicon cantilevers has been investigated as showcase of new optical NEMS sensors for detection of stress, strain and force [23–27]. In view of the guidewire based implanted sensor application, development of sensors with extremely small footprint is an everlasting goal. Optical NEMS sensors with potential of integration of fibre optics as the read-out interface fit into the criteria of design and package of guidewire based implanted sensor. Therefore, novel optical NEMS diaphragm sensors integrated with PhC triple-nano-ring (TNR) resonator are proposed for force and pressure sensing. Performance of optical NEMS diaphragm sensors is investigated in terms of device configurations computationally.

2. Device configuration and modeling methodology

The TNR PhC resonator is formed by three triangular-arranged hexagonal nano-rings with size of 2.87 μm for each ring, as shown in Fig. 1. The nano-rings locate at a diaphragm which have two designs, e.g. either pure single layer of Si with thicknesses of

* Corresponding author. Tel.: +65 6516 5865; fax: +65 6779 1103.
E-mail address: elelc@nus.edu.sg (C. Lee).

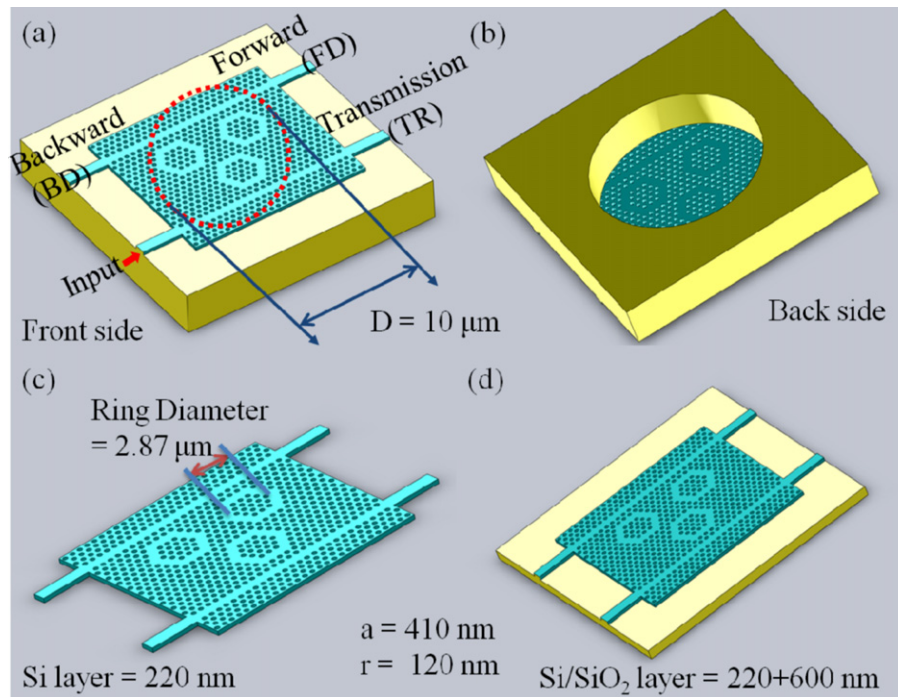


Fig. 1. (a and b) 3-D illustration of the PhC diaphragm sensor using hexagonal triple-nano-ring (TNR) resonator; (c) Si layer diaphragm; (d) Si/SiO₂ layer diaphragm. (For interpretation of the references to colour in the artwork, the reader is referred to the web version of this article.)

220 nm or bilayer of Si and SiO₂ with thicknesses of 220 nm and 600 nm, respectively. The diaphragm of 10 μm in diameter (d) is patterned and released from the 220 nm thick silicon device layer of a silicon-on-insulator (SOI) wafer. Many methods are available to fabricate such structure in the literature, such as deep UV lithography [28,29]. The air holes with lattice constant (*a*) and radius (*r*) are only etched on the silicon device layer to form PhC structure. The lattice constant (*a*) refers to the distance from the centre of a hole to the centre of the next adjacent hole. The nano-rings and the waveguides are made by removing of air holes, indicate “*a*” as the periodicity to form such layouts in the silicon PhC slab of hexagonal lattice. The two horizontally placed nano-rings are separated by three air holes. The 3rd ring is located at the middle of the two horizontal rings with one line of air holes separation between the two horizontal rings and the 3rd ring (Fig. 1(a)). The two waveguides are placed at two sides of the resonator and have two lines of air holes separation with respect from the edge of nano-rings. The input light port located at bottom left is denoted by a red arrow in Fig. 1(a) and the other three output ports are named as transmission (TR), forward drop (FD) and backward drop (BD), respectively. Plane wave expansion (PWE) method is used to calculate the cavity modes of the PhC slab structure. Such approach has been reported by Kitamura et al., in which it has good agreement with measured results [30]. By leveraging this PWE method, we obtain the band gap structure of the 220 nm silicon PhCs slab of hexagonal lattice of air holes. According to the derived band gap map as shown in Fig. 2, the ratio between the *r* and *a* is selected as 0.292. In our case, the air holes have *r* of 0.12 μm and *a* of 0.41 μm, respectively. Those parameters are designed and optimized in order to achieve resonant peak output with high quality factor (Q-factor) at the FD port. The normalized frequency range of first photonic band gap extends from 0.26 to 0.33 in TM polarization electromagnetic wave, i.e., the magnetic field parallel to the surface of silicon slab. The corresponding directions of ΓM and ΓK with respect to hexagonal lattice are indicated in the inset of Fig. 2. The corresponding band gap wavelength range extends from 1.242 to 1.577 μm, which encloses our interested range. For the modeling methodology of

PhC parts of the whole device, a combinational approach of the 2-D finite-difference time-domain (FDTD) method and the effective refractive index (ERI) approximation was deployed to calculate and predict the performance of TNR resonator, and the field distribution of resonant mode in this study. Qiu reported a good agreement between the data derived by this combinational approach and full vector three dimensional (3-D) FDTD method [31]. Furthermore, experimental data have been predicted well by this combinational approach by the other groups as well [32,33].

The PhC structures are quite sensitive with the layout locations of the air holes and the defects. Changing of the physical distance of holes in the PhC resonator will affect the resonant wavelength and lead wavelength shift to a new value. In the applications, external load will introduce the vertical displacement at diaphragm centre and strain in the TNR resonator sensing element region. The load

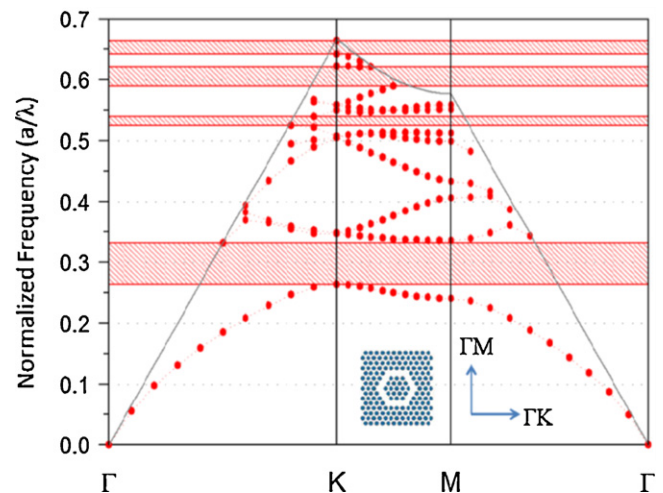


Fig. 2. Band structure of the PhCs structure of hexagonal lattice. (For interpretation of the references to colour in the artwork, the reader is referred to the web version of this article.)

could be a force or pressure depending on the real applications. Finite-element analysis (FEA) is deployed to obtain the deformation data of holes among PhC air-hole array under various loads which are applied at the centre point of the diaphragm. The Young's modulus and Poisson's ratio of Si used in FEA simulation are 130 GPa and 0.3, respectively, while such values are 70 GPa and 0.17 for SiO₂. We further apply the combinational approach of numerical 2-D FDTD and ERI method to simulate the propagation of the electromagnetic waves in the deformed PhC TNR resonator structure in the presence of various applied loads. We expect the resonant peak to vary according to the deformation of TNR resonator. In our previous study [23], we realized that the small shape change of air-holes among the deformed PhC structure brings negligible influence on the output resonant behavior. More importantly, the relative position shift of these air-holes among the deformed PhC structure plays a major role in contribution to the resonant behavior. Thus we recorded the position of holes in the deformed region of diaphragm under force load according to the FEA results, and conducted the 2-D FDTD modeling based on the layout of such deformed TNR resonators.

Moreover, we are interested in the performance of the resonator when the input port is swapped with the BD port in Fig. 2, since the triangle layout of nano-rings is symmetric for nano-rings, but it is not a symmetric feature with respect to the input and output waveguides. Very interestingly, we found out that the forward drop resonant peak is derived at the same wavelength at the new FD port (the TR port in Fig. 2); the only difference is the normalized intensity of the peak. Hence, we name this phenomenon as dual channel reversibility (DCR).

3. Results and discussion

3.1. Characteristics of TNR resonator

The TNR resonators give strong resonant peaks at the FD port, as shown in Fig. 3. The spectra plots are shown in similar fashion but with different location of the resonant peak wavelength for Si layer and Si/SiO₂ layer cases in Fig. 3(a) and (b), respectively. Two major peaks are shown in the transmission spectra and we are more interested in the peak of longer wavelength, since the light intensity ratio of FD port to BD port reaches maximum at this point. From the inset table of Fig. 3, resonant peaks appear at higher wavelength and show higher Q-factor in the Si/SiO₂ case, i.e., 1737 compared with 1602 for the Si layer case. The additional oxide layer in the Si/SiO₂ case can increase the ERI of the Si/SiO₂ bilayer. Thus it can perform better light confinement than the case of Si layer. Hence, a higher Q factor is obtained for the Si/SiO₂ case too. In addition, the intensity ratio of the FD port and BD port are 23.63 and 18.43 for Si/SiO₂ and Si layer, respectively. As a result, the TNR resonator is considered as a channel drop filter since only single output port is activated at the particular wavelength. Fig. 3(c) and (d) is the spectra plot of TNR resonator that the input port and BD port are swapped. From the inset table in the plot we can observe the resonant peaks are exactly the same positions with the case of initial ports allocation. The only differences are the Q-factors of the peaks and some intensity variation. Fig. 4 illustrates the results of continuous wave field distribution of the TNR resonator. The three frames show resonance happening at three transit time points within the TNR resonator. Fig. 4(a) shows the condition that all the three nano-rings are in the active mode. Light comes from the bottom left side and is coupled to the bottom ring first, and then is coupled to the top two rings. Energy exchange happens among each ring, but most of them happens between the top two rings. The bottom ring, showing 90° phase shift with respect to the top two rings, has less portion of importance in the resonant mode. On the other hand, Fig. 4(b)

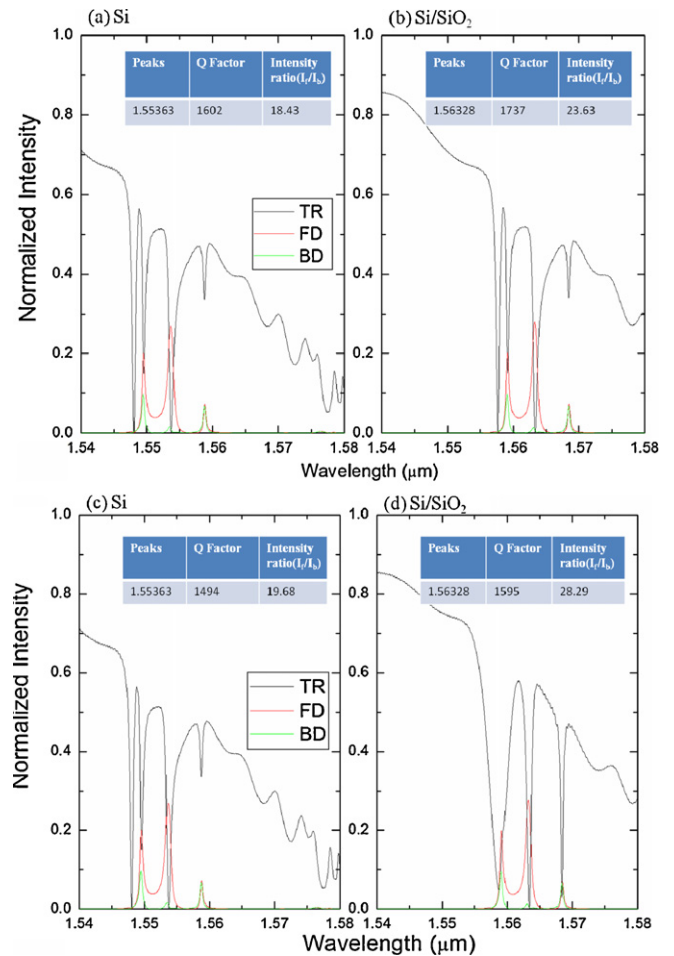


Fig. 3. Spectra of ports FD, BD and TR for TNR channel drop filter: (a) Si layer diaphragm; (b) Si/SiO₂ layer diaphragm. (c) Si layer diaphragm when input port was swapped with BD port and (d) Si/SiO₂ layer diaphragm when input port was swapped with BD port.

and (c) shows cases that only two rings are activated in the resonance. Apparently all the three resonant modes contribute to the forward drop mechanism mainly. Thus this unique TNR resonator demonstrates the channel drop filter behavior. On the other hand, the unique feature of the TNR resonator is the symmetric resonance behavior. It leads to the same output spectra obtained at FD, BD and TR ports, when the input port is swapped with any one among the three rest ports shown in Fig. 1(a). The continuous wave simulation plot of the TNR resonator with input port swapped with BD port is shown in Fig. 4(d–f). We can observe similar trends of the three resonance modes compare with the normal case but the field distribution show certain distinctive between these two input ports design. Therefore, the selected resonance wavelengths appear the same but the Q-factors and the output intensities do not, as shown in Fig. 3.

3.2. Force sensing characteristics of TNR resonator

The mechanical deformation or displacement of the diaphragm can be introduced by external applied force. Hence, force sensing can be explored by using a diaphragm with the TNR resonator on the Si layer. Fig. 5 illustrates the FEM modeling of the Si-diaphragm under various force loads. Different forces are applied at the centre point of the Si diaphragm. Due to the symmetric nature of circular diaphragm, linear relationship of the centre displacement along the normal direction of the diaphragm and the applied force is

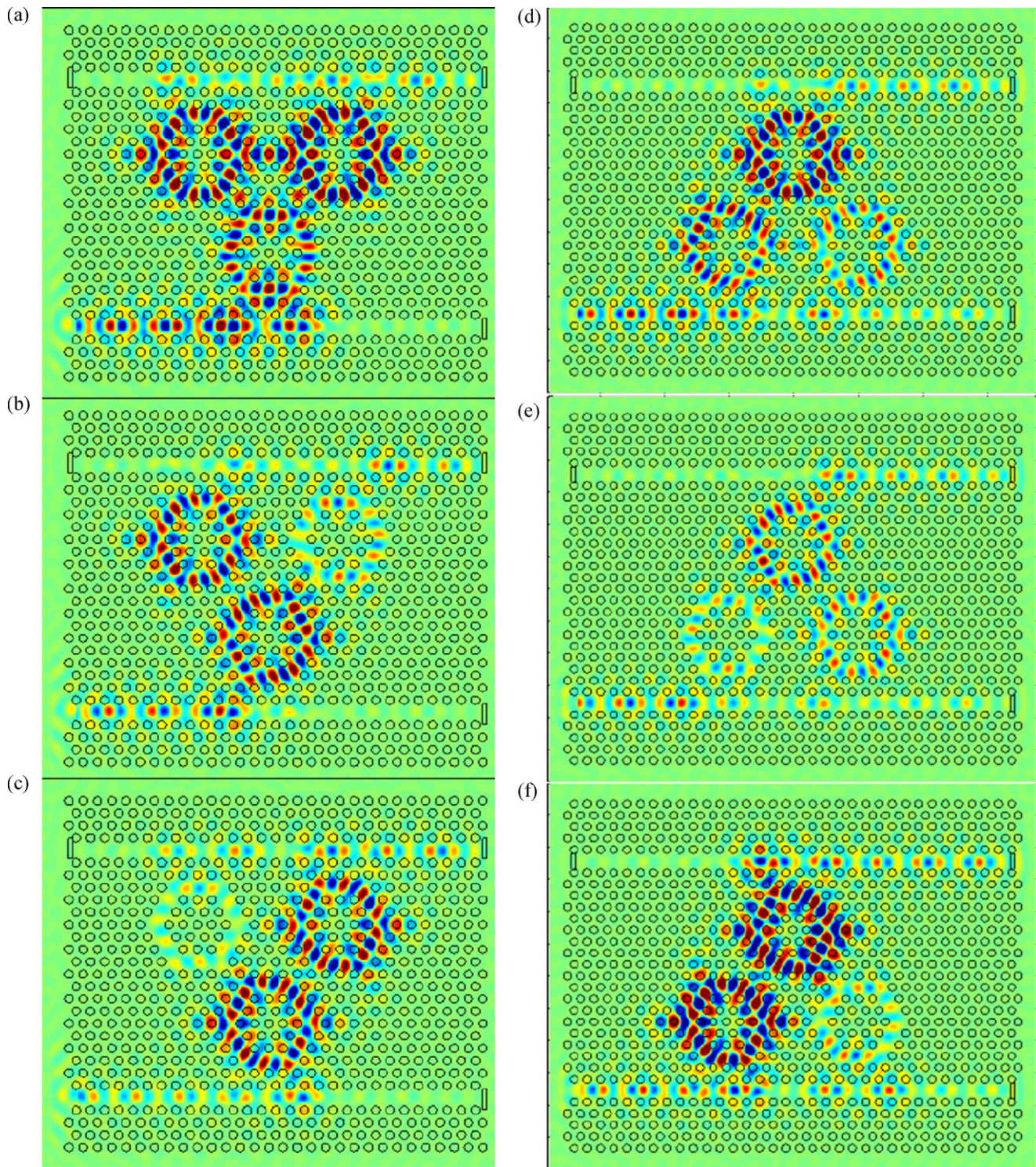


Fig. 4. Images of continuous wave field distribution for TNR resonators. (a–c) show three modes of field distribution under the resonance; (d–f) show three similar modes of field distribution under the resonance when input port swaps with BD port.

obtained in the FEM modeling results. Fig. 6 shows the resonant peak plot obtained at the FD port of the TRN resonator. The resonant peak of the no-load case falls at 1553.63 nm with a Q-factor of 1602. As we increase the constant loading force at the centre of the Si-diaphragm, the FD resonant peak shifts accordingly. It shows that the FD resonant peak shifts to the higher wavelength region as the applied force increases. Furthermore, the resonant peaks maintain similar Q-factor value as the load force increases

and reaches about 20 μN . It implies a wide force-sensing range of the Si-diaphragm as a NEMS sensor. Fig. 7(a) illustrates the relationship of the resonant peak wavelength versus the applied force on the Si-diaphragm. The resonant peak wavelength is characterized as a function of applied force and we find that the 2nd-order polynomial fitting curve (red lines) is in a good agreement with the derived data points. However, from the 2nd-order polynomial fitting curve, we can further divide those data points into two groups. Within

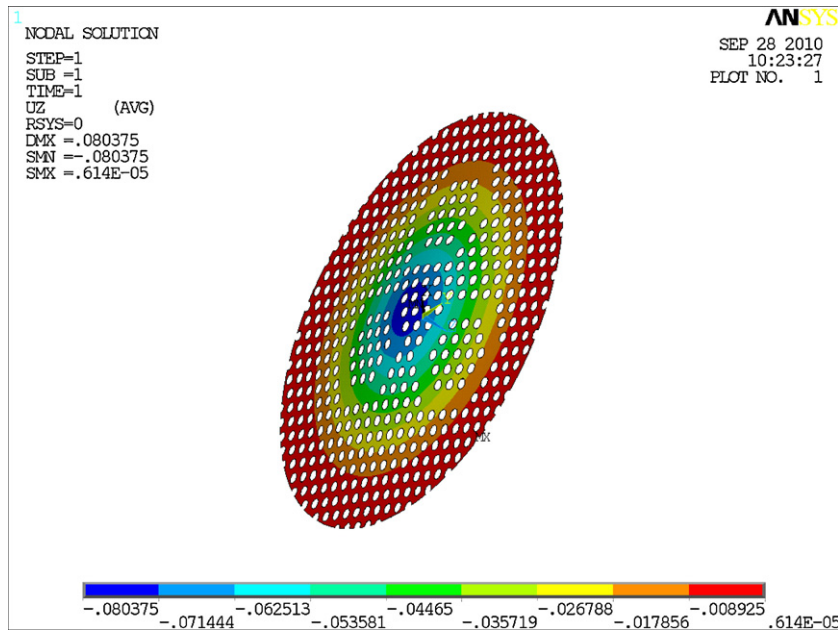


Fig. 5. Side view of FEA simulation result of Si layer diaphragm under 10 μN applied force.

these two regions, the blue dotted fitting lines in Fig. 7(a) present linear relationship approximately. We can estimate force-sensing sensitivity in these two regions accordingly. More specifically, the slope of the blue dotted fitting line within the region of 0–10 μN is derived as 0.0125 nm/ μN , while such slope is 0.118 nm/ μN in the region of 10–20 μN . As a result, if the wavelength measurement resolution is 0.1 nm [23], the minimum detectable force is calculated as 8 μN and 0.847 μN in the region of 0–10 μN and 10–20 μN , respectively. On the other hand, such data point out the resonant wavelength shift introduced by the same incremental force will be larger when the deformation of the Si-diaphragm reaches a certain threshold level. It can be explained as the resonance among the TNR is close to completely vanishing point when the Si-diaphragm deformation is approaching this threshold level. Fig. 7(b) illustrates the Q-factor change with respect to applied external force. We can observe that the initially Q-factor is around 1600 and keep decreasing as the load increases. We can then conclude that as higher applied force introduces larger deformation, the resonance condition would be destroyed.

When the Si-diaphragm deformation achieves the threshold level or even beyond such value, the resonance among the TNR is destroyed and the Q-factor of resonant peak reduced significantly. In such case, the Si-diaphragm with TNR resonator is not good enough to be used as a sensor.

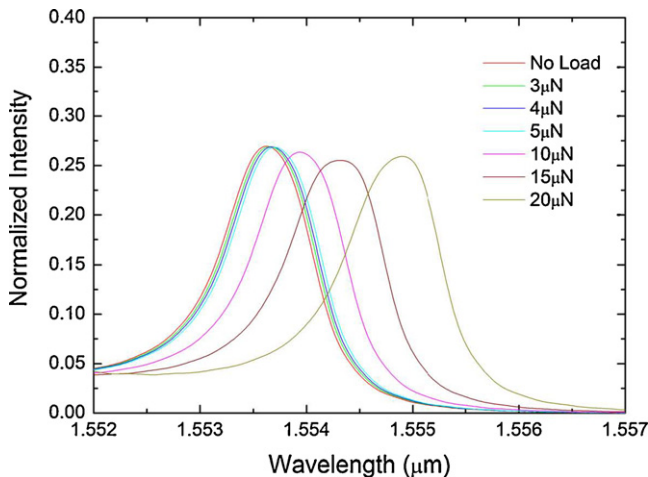


Fig. 6. Resonant wavelength peak at the backward drop (BD) port under various force loads of Si layer diaphragm force sensor.

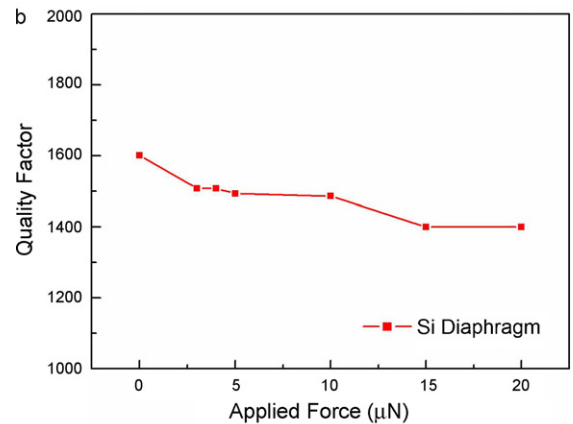
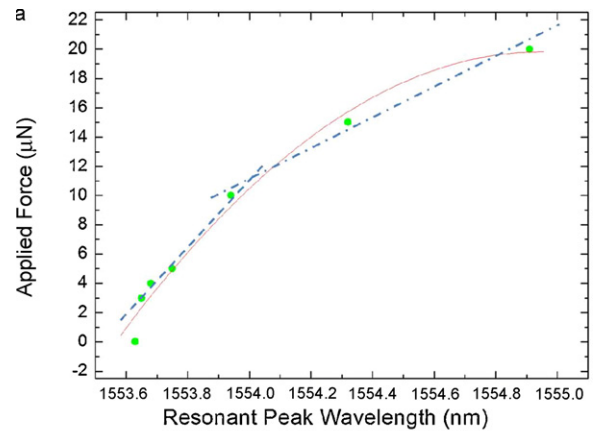


Fig. 7. (a) Resonant wavelength as functions applied force (b) Q-factor versus applied force of Si layer diaphragm force sensor. (For interpretation of the references to colour in the artwork, the reader is referred to the web version of this article.)

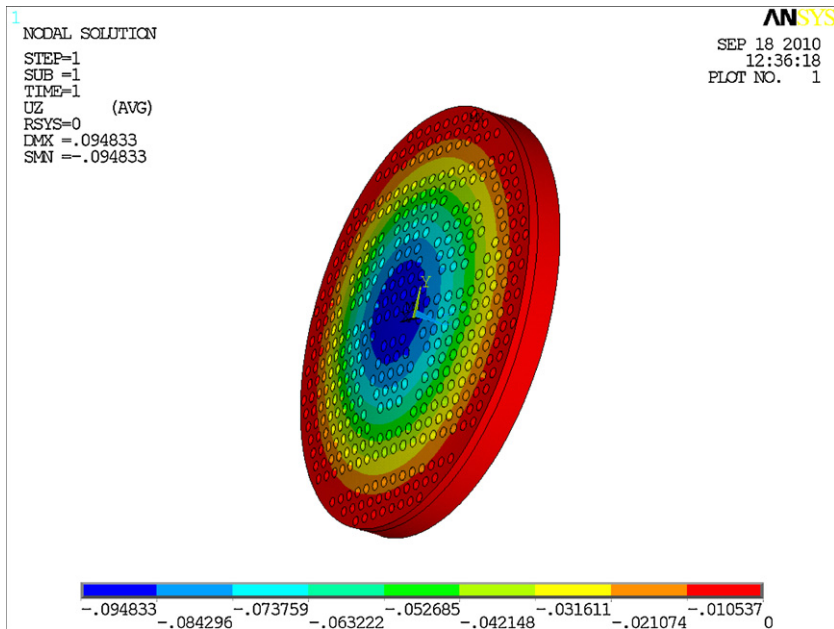


Fig. 8. Side view of FEA simulation result of Si/SiO₂ layer diaphragm under 30 MPa applied pressure.

3.3. Pressure sensing characteristics of TNR resonator

When the SiO₂ layer is retained underneath the Si layer, a Si/SiO₂ bilayer diaphragm is created and it enables the pressure sensing. Fig. 8 illustrates the FEM modeling of the Si/SiO₂ bilayer diaphragm under various pressure loads. The stiffness of bilayer structure is higher than the Si layer case, hence, the deformation of the Si/SiO₂ bilayer diaphragm is much smaller than the Si-diaphragm case. However, similar linear relationship between the loaded pressure and the centre normal displacement of the diaphragm is obtained. Fig. 9 shows the resonant peak plot obtained at the FD port of the TRN resonator in the case of Si/SiO₂ bilayer diaphragm. The resonant peak of the no-load case falls at 1563.28 nm with the Q-factor of 1737. The first two pressure data correspond to the force loads of 10 μN and 20 μN, i.e., the force loads investigated in the previous Si-diaphragm case, but no wavelength shift is observed since the deformation is negligible. As the load pressure increases, same red shift behavior of the resonant wavelength is observed and obtained Q-factor values do not change, in which it represents that good light confinement is still valid. Fig. 10(a) illustrates

the relationship of the resonant peak wavelength with the applied pressure in the case of the Si/SiO₂ diaphragm. A 2nd-order polynomial curve (green line) fits the derived data well. In order to evaluate the pressure-sensing sensitivity in the linear region, we divide the

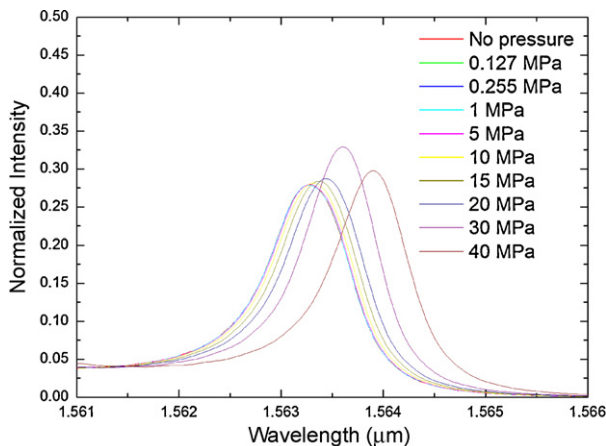


Fig. 9. Resonant wavelength peak at the backward drop (BD) port under various pressure loads of Si/SiO₂ layer diaphragm pressure sensor.

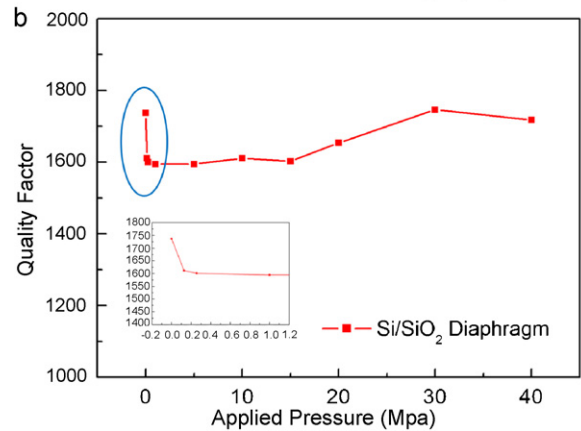
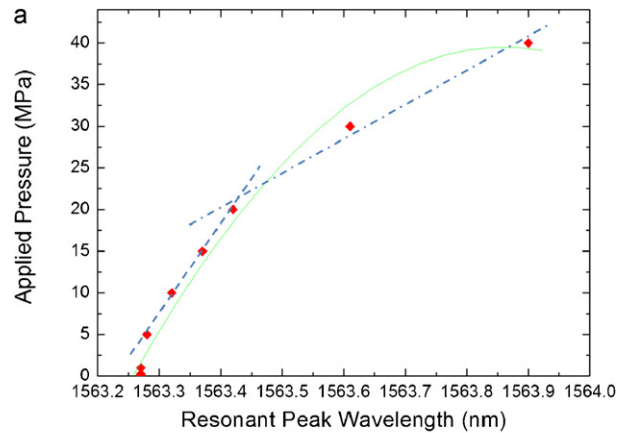


Fig. 10. (a) Resonant wavelength as functions applied pressure (b) Q-factor versus applied pressure of Si/SiO₂ layer diaphragm pressure sensor. (For interpretation of the references to colour in the artwork, the reader is referred to the web version of this article.)

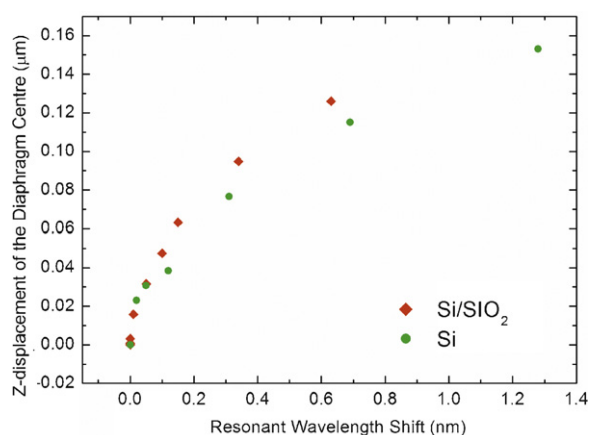


Fig. 11. Resonant wavelength as functions of Z-displacement for two diaphragm sensors.

data into group of 5–20 MPa and group of 20–40 MPa. By taking the blue dotted fitting lines in these two regions, we derived the slope of 0.0094 nm/MPa in the pressure range of 5 MPa–20 MPa, and 0.024 nm/MPa for range of 20–40 MPa. Therefore, the corresponding minimum detectable pressure is calculated as 10.64 MPa and 4.17 MPa, respectively. Fig. 10(b) illustrates the Q-factor change with respect to applied external pressure. Different from the force sensor, the Q-factor has a significant increase at 30 MPa pressure load. Hence we can conclude that the bottom layer of SiO₂ in the pressure sensor provides better light confinement than single Si layer force sensor.

3.4. Sensitivity comparison

So far the resonant wavelength is characterized and plotted as functions of applied force and pressure. In fact, deformation at the centre of diaphragm along the normal direction, i.e., Z-direction, is introduced by such force and pressure loads. To compare the sensing sensitivity of these two TNR resonator diaphragm sensors, the resonant wavelength shift was derived according to the Z-displacement measured at the centre of the diaphragm created by either force load or pressure load. As shown in Fig. 11, in the range of small Z-displacement, e.g. smaller than 0.03 μm, both diaphragm sensors show the same relationship in the derived curves. From the slope of the curves in this region, the derived minimum detectable change in the Z-displacement is 49 nm when the resonant peak wavelength shifts for 0.1 nm. In the range of large Z-displacement,

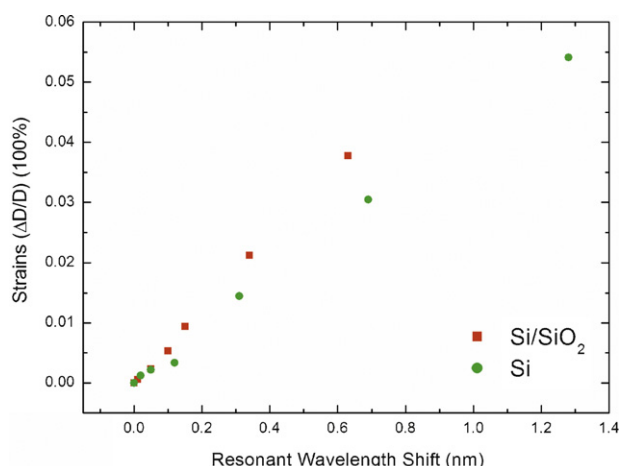


Fig. 12. Resonant wavelength as functions of strains for two diaphragm sensors.

Si diaphragm shows better sensitivity in terms of resonant wavelength shift under the same incremental Z-displacement. Briefly speaking, the derived data of 49 nm displacement at the centre of a 10 μm diaphragm refers to a good sensing capability in the NEMS field. Resonant wavelength shift versus the diaphragm strains are plotted as shown in Fig. 12. Linear relationship is found for both the Si and Si/SiO₂ diaphragm sensors. The minimum detectable strain is calculated as 0.00427% and 0.00608% under 0.1 nm of wavelength shift for Si-layer diaphragm and Si/SiO₂ bilayer diaphragm, respectively.

4. Conclusion

In this paper, we proposed a photonic crystal based triple-nanoring (TNR) resonator and the micro force and pressure sensing applications integrated with the Si and Si/SiO₂ diaphragm. The significant forward channel drop features of the TNR resonator gives strong resonant peak with quality factor of 1602 and 1737 for Si and Si/SiO₂ diaphragm, respectively. Higher effective refractive index (ERI) of the Si/SiO₂ bilayer diaphragm leads better light confinement which results in higher Q-factor and higher intensity ratio of forward drop to backward drop. The 2nd-order-polynomial fitting curve is obtained for the curves of the resonant wavelength versus the applied loads for both the cases. Two linear fitting lines are applied on the derived data points to get slope of wavelength shift versus applied load. Hence, the Si diaphragm device shows wide sensing range and gives minimum detectable force of 0.847 μN in the region of 15–20 μN. Si/SiO₂ diaphragm based pressure sensor gives minimum detectable pressure of 4.17 MPa in the region of applied pressure from 20 to 40 MPa. From the derived wavelength shift versus a given centre displacement of the diaphragm, Si diaphragm based sensor shows higher sensitivity than Si/SiO₂ diaphragm sensor. Present designs reveal interesting device configurations for pressure and force sensing with ultracompact footprint, e.g. the sensing area is as small as 10 μm. With further integration of fibre optics, the investigated device concepts could find particular applications in the guided-wire based implanted biomedical sensors.

Acknowledgements

This work was supported in research grant of University Research Fund R-263-000-475-112 and Academic Research Committee Fund MOE2009-T2-2-011 (R-263000598112) at the National University of Singapore, and A*-STAR, SERC Grant Nos. 0921010049 and 1021520013. Li thanks research scholarship provided National University of Singapore. Authors thank valuable advice from Prof. Gengchiao Liang and Prof. Aaron Danner. Authors also thank the technical support from staff at Centre for Integrated Circuit Failure Analysis & Reliability (CICFAR), Centre for Optoelectronics and Computational Nanoelectronics & Nanodevices Laboratory of National University of Singapore.

References

- [1] A.A. Barlian, W.-T. Park, J.R. Mallon, A. Rastegar, B.L. Pruitt, Review: semiconductor piezoresistance for microsystems, *Proc. IEEE* 97 (3) (2009) 513–552.
- [2] C. Stampfer, T. Helbling, D. Oberfell, B. Schoberle, M.K. Tripp, A. Jungen, S. Roth, V.M. Bright, C. Hierold, Fabrication of single-walled carbon-nanotube-based pressure sensors, *Nano Lett.* 6 (2) (2006) 233–237.
- [3] C. Hierold, A. Jungen, C. Stampfer, T. Helbling, Nano electromechanical sensors based on carbon nanotubes, *Sens. Actuators A* 136 (1) (2007) 51–61.
- [4] A.K. Wanekaya, W. Chen, N.V. Myung, A. Mulchandani, Nanowire-based electrochemical biosensors, *Electroanalysis* 18 (6) (2006) 533–550.
- [5] Z. Gao, A. Agarwal, A.D. Trigg, N. Singh, C. Fang, C.-H. Tung, Y. Fan, K.D. Budharaju, J. Kong, Silicon nanowire arrays for label-free detection of DNA, *Anal. Chem.* 79 (2007) 3291–3297.
- [6] P. Neuzil, C.C. Wong, J. Reboud, Electrically controlled giant piezoresistance in silicon nanowires, *Nano Lett.* 10 (4) (2010) 1248–1252.

- [7] B.W. Soon, P. Neuzil, C.C. Wong, J. Reboud, H.H. Feng, C. Lee, Ultrasensitive nanowire pressure sensor makes its debut, in: Proc. Eurosens. XXIV, September 5–8, Linz, Austria, 2010.
- [8] Y. Haga, M. Esashi, Biomedical microsystems for minimally invasive diagnosis and treatment, Proc. IEEE 92 (2004) 98–114.
- [9] R.A.M. Receveur, W.F. Lindemans, N.F. de Rooij, Microsystem technologies for implantable applications, J. Micromech. Microeng. 17 (2007) R50–R80.
- [10] K.C. Katuri, S. Asrani, M.K. Ramasubramanian, Intraocular pressure monitoring sensors, IEEE Sens. J. 8 (1) (2008) 12–19.
- [11] L. Lou, C. Lee, G.X. Xu, R.K. Kotlanka, L. Shao, W.-T. Park, D.L. Kwong, Design and characterization of MEMS flow sensors using silicon nanowires, Nanosci. Nanotechnol. Lett., doi:10.1166/nnl.2011.1160.
- [12] E. Yablonovitch, Inhibited spontaneous emission in solid-state physics and electronics, Phys. Rev. Lett. 58 (1987) 2059–2062.
- [13] S. John, Strong localization of photons in certain disordered dielectric superlattices, Phys. Rev. Lett. 58 (1987) 2486–2489.
- [14] S. Fan, P.R. Villeneuve, J.D. Joannopoulos, H.A. Haus, Channel drop filters in photonic crystals, Opt. Express 3 (1998) 4–11.
- [15] C.C. Chen, H.D. Chien, P.G. Luan, Photonic crystal beam splitters, Appl. Opt. 43 (2004) 6188–6190.
- [16] B.J. Luff, R.D. Harris, J.S. Wilkinson, R. Wilson, D.J. Schiffrin, Integrated-optical directional coupler biosensor, Opt. Lett. 21 (1996) 618–620.
- [17] A. Martinez, F. Cuesta, J. Marti, Ultrashort 2-D photonic crystal directional couplers, IEEE Photon. Technol. Lett. 15 (2003) 694–696.
- [18] H.-T. Chien, C. Lee, H.-K. Chiu, K.-C. Hsu, C.-C. Chen, J.A. Ho, C. Chou, The comparison between the graded photonic crystal coupler and various couplers, IEEE J. Lightwave Technol. 27 (7) (2009) 2570–2574.
- [19] B.E. Little, J. Foresi, G. Steinmeyer, E.R. Thoen, S.T. Chu, H. Haus, E. Ippen, W.L.C. Kimberling, W. Greene, Ultra-compact Si-SiO₂ microring resonator optical channel dropping filters, IEEE Photon. Technol. Lett. 10 (1998) 549–551.
- [20] D.G. Rabus, M.U. Hamacher Troppenz, H. Heidrich, High-Q channel-dropping filters using ring resonators with integrated SOAs, IEEE Photon. Technol. Lett. 14 (2002) 1442–1444.
- [21] A. Melloni, R. Costa, P. Monguzzi, M. Martinelli, Ring-resonator filters in silicon oxynitride technology for dense wavelength-division multiplexing systems, Opt. Lett. 28 (2003) 1567–1569.
- [22] T. Barwicz, M.A. Popovic, P.T. Rakich, M.R. Watts, H.A. Haus, E.P. Ippen, H.I. Smith, Microring-resonator-based add-drop filters in SiN: fabrication and analysis, Opt. Express 12 (2004) 1437–1442.
- [23] C. Lee, R. Radhakrishnan, C.-C. Chen, J. Li, J. Thillaigovindan, N. Balasubramanian, Design and modeling of a nanomechanical sensor using silicon photonic crystal, IEEE J. Lightwave Technol. 26 (April) (2008) 839–846.
- [24] C. Lee, J. Thillaigovindan, Optical nanomechanical sensor using a silicon photonic crystals cantilever embedded with a nanocavity resonator, Appl. Opt. 48 (2009) 1797–1803.
- [25] W. Xiang, C. Lee, Nanophotonics sensor based on microcantilever for chemical analysis, IEEE J. Sel. Top. Quantum Electron. 15 (2009) 1323–1326.
- [26] T.T. Mai, F.-L. Hsiao, C. Lee, W. Xiang, C.-C. Chen, W.K. Choi, Optimization and comparison of photonic crystal resonators for silicon microcantilever sensors, Sens. Actuators A. 165 (2011) 16–25.
- [27] B. Li, F.L. Hsiao, C. Lee, Computational characterization of photonic crystal cantilever sensor using hexagonal dual-nano-ring based channel drop filter, IEEE Trans. Nanotechnol., doi:10.1109/TNANO.2010.2079942.
- [28] W. Bogaerts, P. Dumon, V. Wiaux, S. Beckx, D. Taillaert, B. Luyssaert, J.V. Campenhout, P. Biensman, D.V. Thourhout, Nanophotonic waveguides in silicon-on-insulator fabricated with CMOS technology, J. Lightwave Technol. 23 (1) (2005).
- [29] H.-T. Chien, C. Lee, H.-K. Chiu, K.-C. Hsu, C.-C. Chen, J.A. Ho, C. Chou, The comparison between the graded photonic crystal coupler and various couplers, J. Lightwave Technol. 27 (14) (2009).
- [30] M. Kitamura, S. Iwamoto, Y. Arakawa, Enhanced light emission from an organic photonic crystal with a nanocavity, Appl. Phys. Lett. 87 (2005) 151119.
- [31] M. Qiu, Effective index method for the heterostructure-slab-waveguides-based two-dimensional photonic crystals, Appl. Phys. Lett. 81 (2002) 1163.
- [32] W. Zheng, M. Xing, G. Ren, S.G. Johnson, W. Zhou, W. Chen, L. Chen, Integration of a photonic crystal polarization beam splitter and waveguide bend, Opt. Express 17 (2009) 8657–8668.
- [33] Y. Chassagneux, R. Colombelli, W. Maineults, S. Barbieri, S.P. Khanna, E.H. Linfield, A.G. Davies, Predictable surface emission patterns in terahertz photonic-crystal quantum cascade lasers, Opt. Express 17 (2009) 9492–9502.

Biographies

Bo Li received the B.Sc. degree from the Department of Electrical and Computer Engineering at the National University of Singapore in 2009. He is currently working toward his PhD degree at the same university.

Chengkuo Lee received the M.S. degree in materials science and engineering from National Tsing Hua University, Hsinchu, Taiwan, in 1991, the M.S. degree in industrial and system engineering from Rutgers University, New Brunswick, NJ, in 1993, and the Ph.D. degree in precision engineering from The University of Tokyo, Tokyo, Japan, in 1996. He worked as a Foreign Researcher in the Nanometerscale Manufacturing Science Laboratory of the Research Center for Advanced Science and Technology, The University of Tokyo, from 1993 to 1996. He had also worked in the Mechanical Engineering Laboratory, AIST, MITI of Japan as a JST Research Fellow in 1996. Thereafter, he became a Senior Research Staff Member of the Microsystems Laboratory, Industrial Technology Research Institute, Hsinchu, Taiwan. In September 1997, he joined Metrodyne Microsystem Corporation, Hsinchu, Taiwan, and established the MEMS device division and the first micromachining fab for commercial purposes in Taiwan. He was the Manager of the MEMS device division between 1997 and 2000. He was an Adjunct Assistant Professor in the Electro-physics Department of National Chiao Tung University, Hsinchu, Taiwan, in 1998, and an Adjunct Assistant Professor in the Institute of Precision Engineering of National Chung Hsing University, Taichung, Taiwan, from 2001 to 2005. In August 2001, he cofounded Taiwan's Asia Pacific Microsystems, Inc., where he first became Vice President of R&D, before becoming Vice President of the optical communication business unit and Special Assistant to the Chief Executive Officer in charge of international business and technical marketing for the MEMS foundry service. From 2006 to 2009, he was a Senior Member of the Technical Staff at the Institute of Microelectronics, A*Star, Singapore. He has been an Assistant Professor in the Department of Electrical and Computer Engineering, National University of Singapore, Singapore, since December 2005. He is the coauthor of *Advanced MEMS Packaging* (McGraw-Hill, 2010). He has contributed to more than 130 international conference papers and extended abstracts and 80 peer-reviewed international journal articles in the fields of MEMS, nanophotonics, and nanotechnology. He is also the holder of nine U.S. patents.